Vol 18 No 10, October 2009
1674-1056/2009/18(10)/4083–11

Chinese Physics B

© 2009 Chin. Phys. Soc.
and IOP Publishing Ltd

Simulation of natural convection under high magnetic field by means of the thermal lattice Boltzmann method*

Zhong Cheng-Wen(钟诚文)[a)†], Xie Jian-Fei(解建飞)[a)‡], Zhuo Cong-Shan(卓从山)[a)], Xiong Sheng-Wei(熊生伟)[a)], and Yin Da-Chuan(尹大川)[b)]

[a)] *National Key Laboratory of Aerodynamic Design and Research, Northwestern Polytechnical University, Xi'an* 710072, *China*
[b)] *Faculty of Life Science, Key Laboratory for Space Bioscience and Biotechnology, Northwestern Polytechnical University, Xi'an* 710072, *China*

(Received 9 October 2008; revised manuscript received 13 June 2009)

The thermal lattice Boltzmann method (TLBM), which was proposed by J. G. M. Eggels and J. A. Somers previously, has been improved in this paper. The improved method has introduced a new equilibrium solution for the temperature distribution function on the assumption that flow is incompressible, and it can correct the effect of compressibility on the macroscopic temperature computed. Compared to the previous method, where the half-way bounce back boundary condition was used for non-slip velocity and temperature, a non-equilibrium extrapolation scheme has been adopted for both velocity and temperature boundary conditions in this paper. Its second-order accuracy coincides with the ensemble accuracy of lattice Boltzmann method. In order to validate the improved thermal scheme, the natural convection of air in a square cavity is simulated by using this method. The results obtained in the simulation agree very well with the data of other numerical methods and benchmark data. It is indicated that the improved TLBM is also successful for the simulations of non-isothermal flows. Moreover, this thermal scheme can be applied to simulate the natural convection in a non-uniform high magnetic field. The simulation has been completed in a square cavity filled with the aqueous solutions of KCl (11wt%), which is considered as a diamagnetic fluid with electrically low-conducting, with Grashof number $Gr=4.64\times10^4$ and Prandtl number $Pr=7.0$. And three cases, with different cavity locations in the magnetic field, have been studied. In the presence of a high magnetic field, the natural convection is quenched by the body forces exerted on the electrically low-conducting fluids, such as the magnetization force and the Lorentz force. From the results obtained, it can be seen that the quenching efficiencies decrease with the variation of location from left, symmetrical line, to the right. These phenomena originate from the different distributions of the magnetic field strengths in the zones of the symmetrical central line of the magnetic fields. The results are also compared with those without a magnetic field. Finally, we can conclude that the improved TLBM will enable effective simulation of the natural convection under a high magnetic field.

Keywords: thermal lattice Boltzmann method, natural convection, magnetization force, Lorentz force

PACC: 0340G, 0570, 4725Q

1. Introduction

The lattice-gas cellular automata (LGCA) and the lattice Boltzmann method (LBM) are relatively new and promising methods for the numerical solution of partial differential equations,[1] which can utilize parallel computers to study transport phenomena. The LBM is a derivative of the lattice gas automata (LGA) method; therefore, it inherits some advantages of LGA over traditional computational methods.[2] It is parallel with LBM in nature due to the locality of particle interaction and the transport of particle information, so it is well suited to massively parallel computing. Moreover, the algorithm of this method is a conservation form in nature too, which can enhance its numerical stability as compared with traditional computational methods. The other advantages of LBM, such as numerical accuracy, numerical robustness, flexibility with respect to complex boundaries, and computational efficiency, have also demonstrated the qualification for a new numerical method of computational fluid dynamics (CFD).

*Project supported by the National Natural Science Foundation of China (Grant No 10772150), the Aeronautical Science Fund of China (Grant No 20061453020) and Foundation for Basic Research of Northwestern Polytechnical University.
†E-mail: zhongcw@nwpu.edu.cn
‡Corresponding author. E-mail: xiejf0803@gmail.com

The current LBM, however, lacks a satisfactory thermal model for heat transfer problems.[3] We can classify the previous thermal lattice Boltzmann models (TLBMs) into two categories: the multi-speed (MS) approach and the passive-scalar approach. The MS approach is a straightforward extension of the lattice Boltzmann equation (LBE) in isothermal models where only the density distribution function is used.[4−6] Although this approach has been shown to be theoretically possible,[4] previous models suffered severe numerical instability and the temperature variation is limited to a narrow range.[7]

The passive-scalar approach, which can be called the double-distribution function (DDF) method, utilizes the fact that the macroscopic temperature satisfies the same evolution equation as a passive scalar if the viscous heat dissipation and compression work done by the pressure are negligible.[8,9] The flow field and the passive temperature are presented by two sets of distribution functions respectively: one simulates the Navier-Stokes equations, and the other simulates the advection-diffusion equation satisfied by the passive scalar driven by the flow. That is, the temperature is simulated using a separate distribution function which is independent of the density distribution. Compared to the MS approach, it enhances the numerical stability.[8,9] In addition, the accuracy of the passive-scalar model has been verified by several benchmark studies.[9,10]

Eggels and Somers[10] proposed a thermal lattice Boltzmann scheme belonging to the passive-scalar approach,[11] where an additional scalar transport equation is coupled with the momentum equations to simulate the nonisothermal flows. However, the density of the fluid in the equilibrium solution of the temperature distribution function could not strictly satisfy the incompressibility assumption of LBM. Moreover, the half-way bounce back boundary condition used in the method was suitable for the non-slip velocity boundary,[12] but not for the temperature that is a scalar quantity. To cure the upper two points, in this paper, the TLBM proposed in Ref.[10] is improved.

The paper is organized as follows. In Section 2, a new equilibrium solution for the temperature distribution function is proposed to improve the thermal lattice Boltzmann scheme proposed in Ref.[10], and a non-equilibrium extrapolation scheme for both non-slip velocity and temperature is adopted. In order to validate the improved thermal scheme, the natural convection of air in a square cavity is simulated in Section 3. While, in order to apply the improved method to the biological field,[13] the natural convection under a high magnetic field is also investigated in Section 4, because damping of natural convection is very important to grow high-quality crystals. And the results are obtained for three different cases, which are further compared with the magnetic-field-free conditions. Finally, conclusions are drawn in Section 5.

2. Thermal lattice Boltzmann mehtod

2.1. Lattice Boltzmann equation

In this paper we derive the discrete lattice Boltzmann equation from the two-dimensional square D2Q9 model, an MS model (see Fig.1).

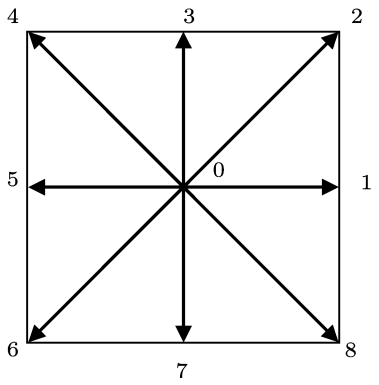


Fig.1. D2Q9 multi-speed model.

The evolution of this scheme contains two steps: a propagation step that shuffles all variables so that mass density N_i at position $\boldsymbol{x}$ can move to position $\boldsymbol{x}+\boldsymbol{c}_i$, and a collision step that redistributes the mass densities among the velocity directions at each grid point locally. Therefore, the scheme can be used to solve the following coupled partial differential equations:[14]

$$\partial_t N_i + \boldsymbol{c}_i \cdot \nabla N_i = \Omega_i(\boldsymbol{N}), \tag{1}$$

where the collision operator $\Omega_i(\boldsymbol{N})$ obeys the basic conservation laws of mass and momentum:

$$\sum\nolimits_i \Omega_i(\boldsymbol{N}) = 0, \quad \sum\nolimits_i \boldsymbol{c}_i \Omega_i(\boldsymbol{N}) = \boldsymbol{f}. \tag{2}$$

The vector $\boldsymbol{f}(\boldsymbol{x},t)$ represents a body force, which contains gravity and magnetic forces, and will be discussed in details in Section 3. The equilibrium solution for mass density distribution function $N_i^{\mathrm{eq}}(\boldsymbol{x},t)$ is as follows:

$$N_i^{\mathrm{eq}}(\boldsymbol{x},t)=\frac{m_i\rho}{24}\left\{1+2\boldsymbol{c}_i\cdot\boldsymbol{u}+3\left(\boldsymbol{c}_i\cdot\boldsymbol{u}\right)^2-\frac{3}{2}\left|\boldsymbol{u}\right|^2-6\nu\left[\left(\boldsymbol{c}_i\cdot\boldsymbol{\nabla}\right)\left(\boldsymbol{c}_i\cdot\boldsymbol{u}\right)-\frac{1}{2}\boldsymbol{\nabla}\cdot\boldsymbol{u}\right]\right\} \tag{3}$$

with $\sum_i N_i=\rho$, $\sum_i \boldsymbol{c}_i N_i=\rho\boldsymbol{u}$ and $m_i=\{4,4,1,4,1,4,1,4,1\}, i=0,\ldots,8$; m_i and ν are weight factors and kinetic viscosity, respectively.

Now consider the staggered formulation of the LBM to specify the collision operator $\Omega_i(\boldsymbol{N})$:

$$N_i\left(\boldsymbol{x}+\frac{1}{2}\boldsymbol{c}_i,t+\frac{1}{2}\right)=N_i\left(\boldsymbol{x}-\frac{1}{2}\boldsymbol{c}_i,t-\frac{1}{2}\right)+\Omega_i(\boldsymbol{N}). \tag{4}$$

With the help of Taylor expansion of $N_i\left(\boldsymbol{x}+\frac{1}{2}\boldsymbol{c}_i,t+\frac{1}{2}\right)$ and $N_i\left(\boldsymbol{x}-\frac{1}{2}\boldsymbol{c}_i,t-\frac{1}{2}\right)$ at $N_i(\boldsymbol{x},t)$, we obtain the expression for collision operator $\Omega_i(\boldsymbol{N})$,

$$\begin{aligned}\Omega_i(\boldsymbol{N})&=N_i\left(\boldsymbol{x}+\frac{1}{2}\boldsymbol{c}_i,t+\frac{1}{2}\right)-N_i\left(\boldsymbol{x}-\frac{1}{2}\boldsymbol{c}_i,t-\frac{1}{2}\right)\\&=\frac{m_i\rho}{12}\left[\left(\boldsymbol{c}_i\cdot\boldsymbol{\nabla}\right)\left(\boldsymbol{c}_i\cdot\boldsymbol{u}\right)-\frac{1}{2}\boldsymbol{\nabla}\cdot\boldsymbol{u}\right]+\frac{m_i}{12}\boldsymbol{c}_i\cdot\boldsymbol{f};\end{aligned} \tag{5}$$

$$N_i\left(\boldsymbol{x}\pm\frac{1}{2}\boldsymbol{c}_i,t\pm\frac{1}{2}\right)=N_i(\boldsymbol{x},t)\pm\frac{1}{2}\Omega_i(\boldsymbol{N}), \tag{6}$$

which can be rewritten in terms of a 9×9 filter matrix E_{ik} and a solution vector $\alpha_k^{\pm}(\boldsymbol{x},t)$ as

$$N_i\left(\boldsymbol{x}\pm\frac{1}{2}\boldsymbol{c}_i,t\pm\frac{1}{2}\right)=\frac{m_i}{24}\sum_{k=1}^{n}E_{ik}\alpha_k^{\pm}(\boldsymbol{x},t),\quad(i=1,\ldots,9). \tag{7}$$

Meanwhile, the expressions of filter matrix E_{ik} and solution vector $\alpha_k^{\pm}(\boldsymbol{x},t)$ are given by

$$E_{ik}=\left[1,2c_{ix},2c_{iy},3\left(c_{ix}^2-\frac{1}{2}\right),6c_{ix}c_{iy},3\left(c_{iy}^2-\frac{1}{2}\right),c_{ix}\left(3c_{iy}^2-1\right),c_{iy}\left(3c_{ix}^2-1\right),3\left(c_{ix}^2-c_{iy}^2\right)^2-2\right], \tag{8}$$

$$\alpha_k^{\pm}(\boldsymbol{x},t)=\begin{bmatrix}\rho,\rho u_x\pm\frac{1}{2}f_x,\rho u_y\pm\frac{1}{2}f_y,\rho u_xu_x+\rho\left(\frac{\pm1-6\nu}{6}\right)(2\partial_x u_x),\\ \rho u_xu_y+\rho\left(\frac{\pm1-6\nu}{6}\right)(\partial_x u_y+\partial_y u_x),\\ \rho u_yu_y+\rho\left(\frac{\pm1-6\nu}{6}\right)(2\partial_y u_y),T_1^{\pm},T_2^{\pm},F^{\pm}\end{bmatrix}. \tag{9}$$

The matrix E_{ik} is formulated in such a way that its inverse E_{ki}^{I} can be determined directly as:

$$E_{ki}^{\mathrm{I}}=\begin{pmatrix}1,c_{ix},c_{iy},\frac{3}{2}c_{ix}^2+\frac{1}{2}c_{iy}^2-1,c_{ix}c_{iy},\frac{3}{2}c_{iy}^2+\frac{1}{2}c_{ix}^2-1,\\ c_{ix}\left(3c_{iy}^2-1\right),c_{iy}\left(3c_{ix}^2-1\right),\frac{3}{2}\left(c_{ix}^2-c_{iy}^2\right)-1\end{pmatrix}^{\mathrm{T}}. \tag{10}$$

According to the equations obtained above, we propose the procedure for evolution of velocity field: First, determine the solution vector $\alpha_k^{-}(\boldsymbol{x},t)$ in terms of $N_i\left(\boldsymbol{x}-\frac{1}{2}\boldsymbol{c}_i,t-\frac{1}{2}\right)$ initialized by equilibrium distribution using Eq.(3),

$$\alpha_k^{-}(\boldsymbol{x},t)=\sum_{i=1}^{n}E_{ki}^{\mathrm{I}}N_i\left(\boldsymbol{x}-\frac{1}{2}\boldsymbol{c}_i,t-\frac{1}{2}\right),\quad(k=1,\ldots,9). \tag{11}$$

The velocity components u_x and u_y can be computed from the components of the body force $\boldsymbol{f}$ that are known, accordingly. Then, separate the shear rates $\partial_x u_x$, $(\partial_x u_y+\partial_y u_x)$ and $\partial_y u_y$ from the total stress. Meanwhile, apply $T_1^{+}=-0.8T_1^{-}$ and $T_2^{+}=-0.8T_2^{-}$ to deal with the third-order terms, and set $F^{+}=0$ for the fourth-order term because of its smallest magnitude. Thirdly, we determine the components of solution vector $\alpha_k^{+}(\boldsymbol{x},t)$ from Eq.(9) and compute the variable $N_i\left(\boldsymbol{x}+\frac{1}{2}\boldsymbol{c}_i,t+\frac{1}{2}\right)$ using Eq.(7). Finally, all variables $N_i\left(\boldsymbol{x}+\frac{1}{2}\boldsymbol{c}_i,t+\frac{1}{2}\right)$ after the collision step are shuffled during the propagation step so that the mass density $N_i\left(\boldsymbol{x}+\frac{1}{2}\boldsymbol{c}_i,t+\frac{1}{2}\right)$ associated with the grid point at position $\boldsymbol{x}$ moves to the grid at position $\boldsymbol{x}+\boldsymbol{c}_i$ to become $N_i\left(\boldsymbol{x}-\frac{1}{2}\boldsymbol{c}_i,t-\frac{1}{2}\right)$ for the next time step.

2.2. Diffusion–advection equation in the lattice Boltzmann scheme

The standard diffusion–advection equation for incompressible flow is[11]

$$\partial_t T + \boldsymbol{u} \cdot \boldsymbol{\nabla} T = a \boldsymbol{\nabla}^2 T, \tag{12}$$

where T and a are temperature and thermal diffusivity, respectively. In analogy to the mass density distribution $N_i(\boldsymbol{x}, t)$, a temperature distribution function $Q_i(\boldsymbol{x}, t)$ is introduced along the velocity direction $\boldsymbol{c}_i$. The evolution of distribution function $Q_i(\boldsymbol{x}, t)$ also obeys the following partial differential equations,

$$\partial_t Q_i + \boldsymbol{c}_i \cdot \boldsymbol{\nabla} Q_i = \Psi_i(\boldsymbol{Q}), \tag{13}$$

where $\Psi_i(\boldsymbol{Q})$ is the operator for temperature. In Eggels and Somers's model for obtaining the evolution of temperature, in the equilibrium solution for temperature distribution function the fluid density is included explicitly, and the assumption that the standard LBM is confined to the case of incompressible flow could not be satisfied strictly. Based on this knowledge, a new equilibrium solution for the temperature distribution function is presented on the assumption that flow is incompressible in this work:

$$Q_i^{\mathrm{eq}}(\boldsymbol{x}, t) = \frac{m_i}{24}\left[T + 2\boldsymbol{c}_i \cdot \boldsymbol{u} T - 2\boldsymbol{c}_i \cdot a \boldsymbol{\nabla} T\right]. \tag{14}$$

The new equilibrium solution does not contain the fluid density as the previous model and can correct the effect of compressibility on computing macroscopic temperature. Accordingly, the definition of the macroscopic temperature is also modified, i.e., $T(\boldsymbol{x}, t) = \sum_i Q_i(\boldsymbol{x}, t)$, and the new thermal model is more consistent with the assumption of incompressibility for the standard LBM. Therefore, the numerical accuracy can also be improved.

Now we deduce the expression for the temperature operator $\Psi_i(\boldsymbol{Q})$. With the help of Taylor expansion, we can obtain

$$Q_i\left(\boldsymbol{x} \pm \frac{1}{2}\boldsymbol{c}_i, t \pm \frac{1}{2}\right) = Q_i(\boldsymbol{x}, t) \pm \frac{m_i}{48}\boldsymbol{c}_i \cdot \boldsymbol{\nabla} T, \tag{15}$$

$$\Psi_i(\boldsymbol{Q}) = \frac{m_i}{24}\boldsymbol{c}_i \cdot \boldsymbol{\nabla} T. \tag{16}$$

Meanwhile, the formulas of the solution vector $\beta_k^{\pm}(\boldsymbol{x}, t)$ and temperature distribution $Q_i\left(\boldsymbol{x} \pm \frac{1}{2}\boldsymbol{c}_i, t \pm \frac{1}{2}\right)$ are given as follows:

$$\beta_k^{-}(\boldsymbol{x}, t) = \sum_{i=1}^{n} E_{ki}^{\mathrm{I}} Q_i\left(\boldsymbol{x} - \frac{1}{2}\boldsymbol{c}_i, t - \frac{1}{2}\right), \quad (k = 1, \ldots, 9); \tag{17}$$

$$Q_i\left(\boldsymbol{x} + \frac{1}{2}\boldsymbol{c}_i, t + \frac{1}{2}\right) = \frac{m_i}{24}\sum_{k=1}^{n} E_{ik}\beta_k^{+}(\boldsymbol{x}, t), \quad (i = 1, \ldots, 9); \tag{18}$$

E_{ik} and E_{ki}^{I} remain to have the forms of Eq.(8) and Eq.(10), respectively. $\beta_k^{\pm}(\boldsymbol{x}, t)$ are expressed below

$$\begin{aligned}
\beta_k^{-}(\boldsymbol{x}, t) &= \left[T, u_x T + \left(\frac{-1 - 4a}{4}\right)\partial_x T, u_y T + \left(\frac{-1 - 4a}{4}\right)\partial_y T, S_1^{-}, S_2^{-}, S_3^{-}, T_1^{-}, T_2^{-}, F^{-}\right], \\
\beta_k^{+}(\boldsymbol{x}, t) &= \left[T, u_x T + \left(\frac{+1 - 4a}{4}\right)\partial_x T, u_y T + \left(\frac{+1 - 4a}{4}\right)\partial_y T, -0.8S_1^{-}, -0.8S_2^{-}, -0.8S_3^{-}, 0, 0, 0\right].
\end{aligned} \tag{19}$$

At this point, we can see that the temperature gradients, i.e., $\partial_x T$ and $\partial_y T$, could be separated from the total flux in terms of the velocity components u_x and u_y that are given. Therefore, we can estimate the evolution of the temperature field as follows: First, we compute the solution vector $\beta_k^{-}(\boldsymbol{x}, t)$ from Eq.(17) using $Q_i\left(\boldsymbol{x} - \frac{1}{2}\boldsymbol{c}_i, t - \frac{1}{2}\right)$ defined in Eq.(14), and determine $\beta_k^{+}(\boldsymbol{x}, t)$ using $\beta_k^{-}(\boldsymbol{x}, t)$ from Eq.(19). Then we can obtain a new temperature distribution $Q_i\left(\boldsymbol{x} + \frac{1}{2}\boldsymbol{c}_i, t + \frac{1}{2}\right)$ from Eq.(18). And finally shuffle $Q_i(\boldsymbol{x}, t)$ at every grid point to end up with $Q_i\left(\boldsymbol{x} - \frac{1}{2}\boldsymbol{c}_i, t - \frac{1}{2}\right)$. It should be noticed that we have set $T_1^{+} = 0$, $T_2^{+} = 0$ and $F^{+} = 0$ to deal with the third-order and fourth-order terms in the solution vector $\beta_k^{+}(\boldsymbol{x}, t)$ for all procedures.

2.3. Boundary conditions

In the tests in Sections 3 and 4, non-slip velocity conditions are imposed on the rigid walls of the cavity. Fixed temperatures (Dirichlet conditions) are prescribed on the vertical walls, whereas the horizontal walls are perfectly insulated (Neumann conditions).

The bounce-back condition is very convenient for dealing with the mass density distribution on the rigid walls; however, it is not suitable to apply it to the temperature that is a scalar quantity for lack of a philosophical idea of momentum exchanges. Therefore, a non-equilibrium extrapolation scheme is introduced, which was proposed by Guo *et al*[15] and Chai *et al*[16] and is the second-order accuracy, the same as the lattice Boltzmann scheme. It is used on the walls for both mass density and temperature distributions. The boundary conditions are as follows:

$$N_{i,\text{wall}} = \overline{N_i^{\text{eq}}}_{\text{wall}} + N_{i,\text{fluid}} - N_{i,\text{fluid}}^{\text{eq}}, \tag{20}$$

$$Q_{i,\text{wall}} = \overline{Q_i^{\text{eq}}}_{\text{wall}} + Q_{i,\text{fluid}} - Q_{i,\text{fluid}}^{\text{eq}}, \tag{21}$$

where $\overline{N_i^{\text{eq}}}_{\text{wall}}$ and $\overline{Q_i^{\text{eq}}}_{\text{wall}}$ are the dummy equilibrium distributions, which are determined by Eqs.(3) and (14) according to the non-slip velocity conditions, and whose densities are equal to the densities of fluid nodes that are close to the walls; $N_{i,\text{fluid}}, N_{i,\text{fluid}}^{\text{eq}}$ and $Q_{i,\text{fluid}}, Q_{i,\text{fluid}}^{\text{eq}}$ are the mass density and temperature distributions, and their equilibrium distributions at the fluid nodes close to the walls, respectively.

3. Natural convection

In order to validate the improved thermal scheme proposed in Section 2, the natural convection of air in a cavity with Ra=10^4, 10^5 and Pr=0.71 is simulated by using the above method. The flow configuration of the test is fairly simple and consists of a two-dimensional square cavity with a hot vertical wall on one side and a cold vertical wall on the opposite side (see Fig.2). The horizontal walls (bottom and top) are considered to be perfectly insulated.

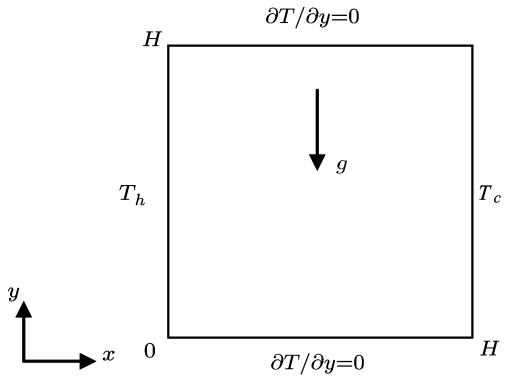


Fig.2. Flow configuration for natural convection.

The two dimensionless parameters, the Rayleigh number (Ra) and the Prandtl number (Pr), which characterize the natural convective flow, are defined as follows:

$$\text{Ra} = \frac{g\beta\Delta T H^3}{\nu a}, \quad \text{Pr} = \frac{\nu}{a}, \tag{22}$$

where g is the gravitational acceleration, β the thermal expansion coefficient, ΔT the temperature difference between the two vertical walls, and H the height (equal to the width) of the cavity. In the test, we apply the Boussinesq approximation to confine the fluid to laminar flow.[17] The body force $\boldsymbol{f}$ which appears in the momentum equation is the buoyancy, which is directly proportional to the temperature variation according to the Boussinesq hypothesis:

$$\boldsymbol{f} = -\rho_{T_0}\boldsymbol{g}\beta\left(T - T_0\right), \tag{23}$$

where $T_0 = \left(T_h + T_c\right)/2$ is the reference temperature.

Figures 3 and 4 show the streamlines and isotherms of the convective flow in the cavity, respectively.

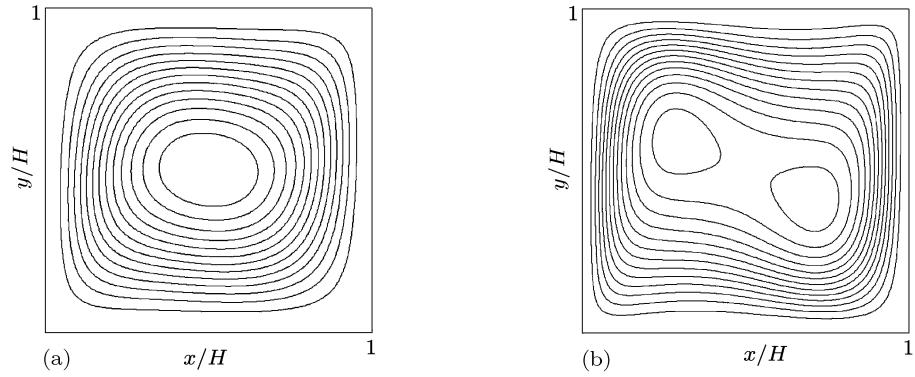


Fig.3. Streamlines of the convective flow in the square cavity, (a) Ra=10^4 and Pr=0.71; (b) Ra=10^5 and Pr=0.71.

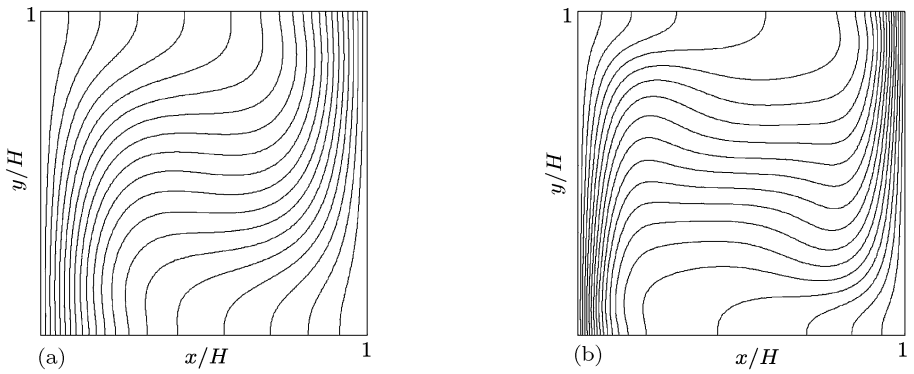


Fig.4. Isotherms of the convective flow in the square cavity, (a) Ra=10^4 and Pr=0.71; (b) Ra=10^5 and Pr=0.71.

Different flow parameters are listed in Table 1: the average heat transfer through the hot wall $\overline{Nu}$, the maximum vertical velocity $v_{\max}/V^*$ along the horizontal center line, the maximum horizontal velocity $u_{\max}/V^*$ along the vertical center line. Here, $\overline{Nu}$ and V^* read,[18]

$$\overline{Nu} = -\frac{1}{\Delta T}\sum_{1}^{H}(\partial_x T)_{x=0}, \quad V^* = \frac{\nu}{\Pr H}. \tag{24}$$

Table 1. Flow parameters for various Rayleigh number (grid 120×120).

Rayleigh number	$\overline{Nu}$	$u_{\max}/V^*$	$v_{\max}/V^*$
10^4			
present work	2.251	19.444	16.012
Barakos *et al*[19]	2.245	19.717	16.262
De Vahl Davis[20]	2.243	19.617	16.178
Fusegi, cited in Ref.[19]	2.302	18.959	16.937
10^5			
present work	4.541	68.473	34.843
Barakos *et al*[19]	4.510	68.746	35.173
De Vahl Davis[20]	4.519	68.59	34.73
Fusegi, cited in Ref.[19]	4.646	65.815	39.169

In Table 1, our results are compared with other published data. The comparisons of the results indicate that the improved TLBM is successful in the simulations of non-isothermal flows. Moreover, this approach will become more useful if the viscous heat dissipation and compression work done by the pressure can be correctly incorporated into the model.

4. Natural convection under a high magnetic field

Based on the simulation of natural convection in Section 3, we simulate the natural convection under the high magnetic field and study the phenomena in this section. The flow configuration of the tests is similar to that of Section 3, except that there is a high magnetic field in the cavity (see Fig.5). The cavity

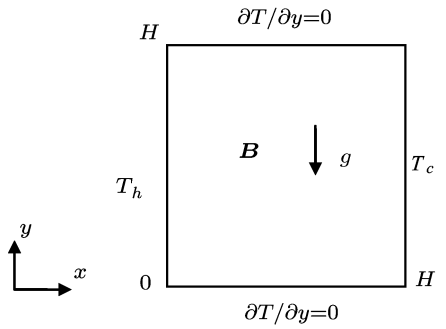


Fig.5. Flow configuration for natural convection under the high magnetic field.

is filled with the aqueous solution of KCl (11wt%), whose electrical conductivity is σ is 15 $\Omega^{-1}\cdot m^{-1}$, and is located in a static high magnetic field (see Fig.6) produced by the superconducting magnet JMTA-16T50. All the results in the present work are taken from simulation with a 101×101 moderate grid and are dimensionless.

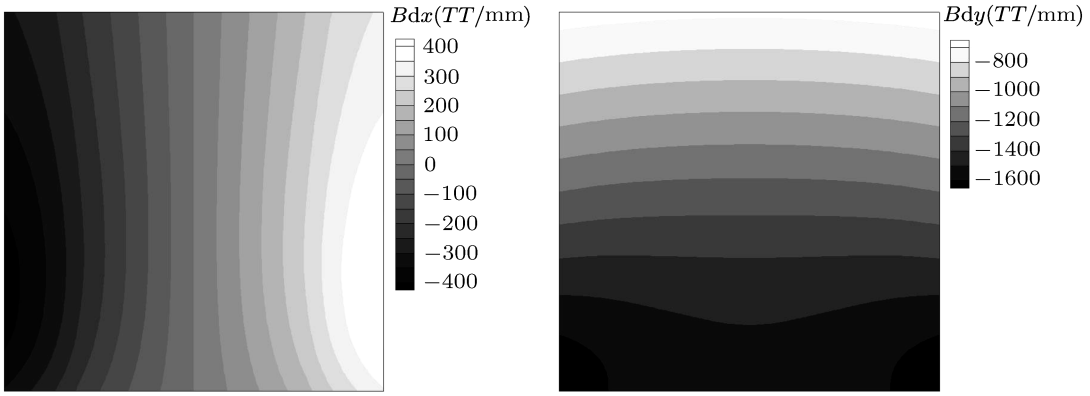


Fig.6. Distribution of magnetic field provided by the superconducting magnet JMTA-16T50: distribution along the x direction (a); distribution along y direction (b).

In all the cases studied, we also apply the Boussinesq approximation to confine the fluid to the laminar flow with Gr=4.64×10^4 and Pr=7.0, where Gr is the Grashof number that represents the ratio of the buoyancy to viscous force acting on a fluid, and we can obtain the Rayleigh number Ra by Ra=Gr Pr.

For the natural convection under the high magnetic field, the body force $\boldsymbol{f}$ appearing in the momentum equation (2) includes the buoyancy $\boldsymbol{f}_g$, magnetization force $\boldsymbol{f}_m$ and Lorentz force $\boldsymbol{f}_z$, which will be shown one by one in the following. The buoyancy $\boldsymbol{f}_g$ has already been discussed in Section 3 and will be skipped over here.

Due to the gradients of a magnetic field, the magnetization force will act on the solution considered as a diamagnetic fluid. It is defined as follows according to the Boussinesq hypothesis:

$$\boldsymbol{f}_m = -(\rho_{T_0}\chi_g/2\mu)\boldsymbol{\nabla}\boldsymbol{B}^2\beta\,(T-T_0)\,, \qquad (25)$$

where χ_g is the mass magnetic susceptibility, μ is the magnetic permeability, and $\boldsymbol{B}$ is the magnetic induction vector.

The magnetization force, which is approximated according to the Boussinesq hypothesis like the buoyancy, will have the same magnitude as the buoyancy under the high magnetic field, that is, they have the similar expressions. Therefore, it is necessary to consider the influence of the magnetization force, which is called the effective factor of gravity p defined as,[21]

$$\begin{aligned} f_g + f_m &= \rho\beta\,(T-T_0)\,(g-(\chi_g/2\mu)\boldsymbol{\nabla}B^2) \\ &= \rho p g\beta\,(T-T_0)\,, \end{aligned}$$

$$p = 1 - \frac{\chi_g}{2\mu g}\boldsymbol{\nabla}B^2. \qquad (26)$$

Next, we will discuss the Lorentz force produced by the flow of the electrically low-conducting fluid:

$$\boldsymbol{f}_z = N\,(\boldsymbol{J}\times\boldsymbol{B})\,, \qquad (27)$$

where the dimensionless parameter N is called the interaction number,[22] which is the ratio of electromagnetic force to the inertia force; $\boldsymbol{J}$ is the current density due to the convection of the solution. N and $\boldsymbol{J}$ are defined as follows:

$$N = \sigma B_0^2 L/\,(\rho_0 V_0)\,, \quad \boldsymbol{J} = \boldsymbol{u}\times\boldsymbol{B} \qquad (28)$$

with σ being the electrical conductivity of the solution, B_0 the characteristic magnetic induction, L the characteristic length, ρ_0 the characteristic density, and V_0 the characteristic velocity.

Here we will give another dimensionless parameter related to the fluid flow under the magnetic field, i.e., magnetic Reynolds number Re$_m$:[23]

$$\mathrm{Re}_m = \frac{V_0 L}{\eta}, \qquad (29)$$

where η is the coefficient of magnetic diffusivity $\eta = \sigma\mu$. Since we have Re$_m \ll 1$ in the tests, the magnetic field induced by the high magnetic field due to the evolution of the velocity field in the electrically low-conducting fluid will not be considered in the simulation. In addition, the magnetic field used in the simulation is a static one and the fluid flow in the cases is not assumed to belong to the magneto-hydrodynamics

in which the velocity field and the magnetic field are coupled to each other. Therefore, the magnetization force and Lorentz force are considered as the undirectional forces that will affect the velocity field; however, the velocity field will not have the reverse effects on the magnetic field. So the electromagnetic induction is ignored in the tests.[24]

In the present work, three different cases are discussed when the cavity is located in different zones of the magnetic field. For the first case, the cavity is located along the symmetry central line of the magnetic field, while, for the second and third cases, the cavities are located in the left and right regions of the symmetry central line of the magnetic field with the radial component of magnetic induction along the negative direction of the horizontal axis, respectively. The above three positions are on the same horizontal line and have the same direction of axial component of magnetic induction along the positive direction of the perpendicular axis. They are labeled as BC, BL, and BR in the following discussions, respectively, and $B0$ is the case without the magnetic field.

4.1. Streamlines

Figure 7 shows the magnetic influences on the streamlines. From Fig.7(a) we can see that the streamlines of the flow are symmetrical in the central region of the cavity without applying the magnetic field, and there are two vortexes in this region, whose rotating directions are clockwise, and the velocity gradients along the vertical walls are larger than those of the horizontal walls. In Fig.7(b), we see that there is only one clockwise vortex rotation at the upper right corner when the cavity is located in the left region of the magnetic field. And the velocity gradients in the upper right region are larger than in the lower left region. In Fig.7(c), a clockwise vortex is observed on the right-hand side of the central line of the cavity, and the velocity gradients are large in all the regions of cavity, especially in the region near the right vertical wall. In Fig.7(d), we see that there is a vortex that rotates clockwise slightly below the horizontal central line of the cavity, and the velocity gradients are larger than those in Fig.7(b), but less than those in Fig.7(c). Figure 7 shows obviously that the magnetic field does lead to different quenching effects for the natural convection.

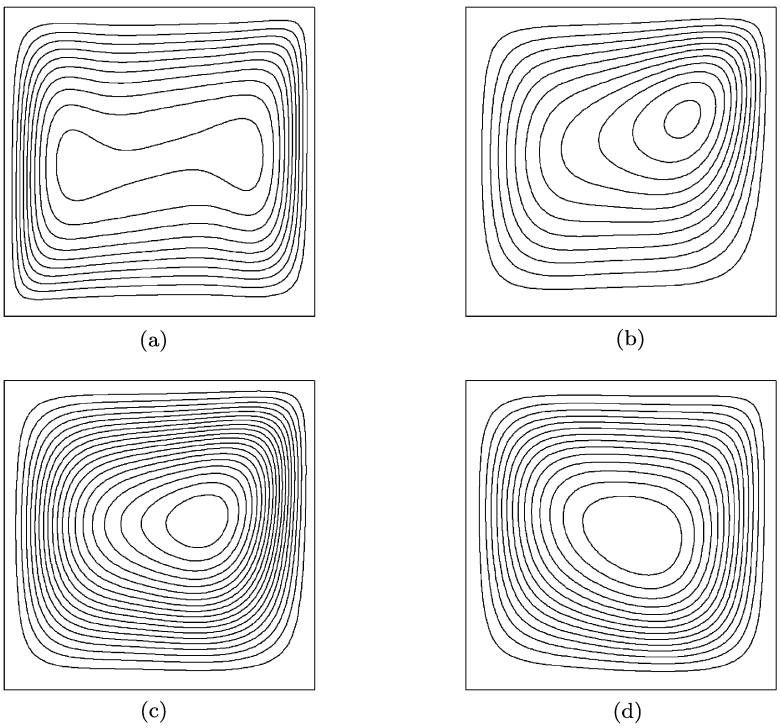


Fig.7. Streamlines in the cavity under the high magnetic field: (a) $B0$, without magnetic field; (b) BL, the cavity located in the left region of the symmetry central line of the magnetic field; (c) BC, the cavity located on the symmetry central line of the magnetic field; (d) BR, the cavity located in the right region of the symmetry central line of the magnetic field.

4.2. Isothermals

Figure 8 shows the isotherms under the high magnetic field when the cavity is located in different zones of the magnetic field. Figure 8(a) shows that the heat exchanges on the vertical walls and the temperature gradients are relatively high in the lower left and upper right corner. The convection, however, dominates the fluid flow in the cavity, and the core region is largely stratified. In Fig.8(b), we can see that the convection has been quenched strongly between the top and bottom walls; however, the heat transmitted from the hot wall to the cold wall is strengthened. In Fig.8(c), it is shown that the temperature gradients are still high near the lower left and upper right regions and the convection in the core region remains, whose region is less than that in Fig.8(a); from Fig.8(d), we see that the temperature gradients in the lower left and upper right corners are larger than those in Fig.8(c), but smaller than those in Fig.8(a), and the convection in the core region is stronger than that in Figs.8(b) and 8(c). Comparing the isotherms in Fig.8, we can draw the same conclusion that the natural convection is quenched strongly in Fig.8(b), to a lesser degree in Fig.8(c), and the least in Fig.8(d).

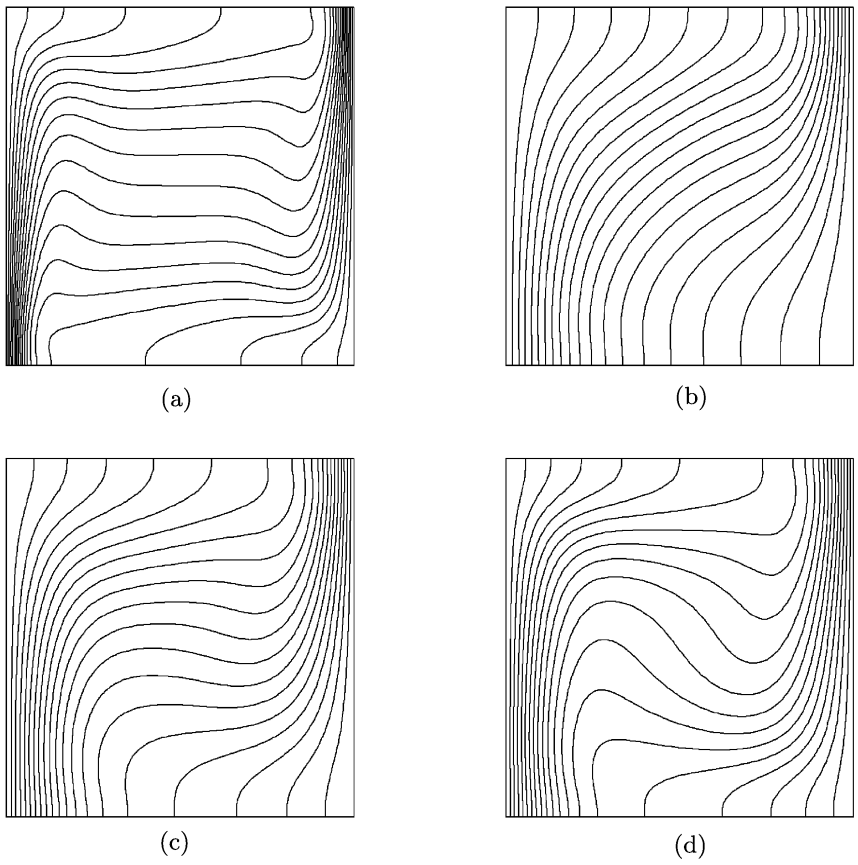


Fig.8. Isotherms under the high magnetic field: (a) $B0$, without the magnetic field; (b) BL, the cavity located in the left region of the symmetry central line of the magnetic field; (c) BC, the cavity located on the symmetry central line of the magnetic field; (d) BR, the cavity located in the right region of the symmetry central line of the magnetic field.

4.3. Velocity profiles

Figures 9 and 10 show the horizontal velocity u along a vertical center line and the vertical velocity v along a horizontal center line.

As shown in Fig.9, the vertical component of velocity is quenched largely due to the existence of high magnetic field. The quenching of vertical velocity decreases through BL, BC to BR.

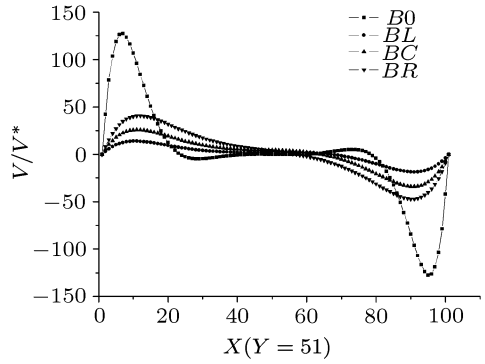


Fig.9. The vertical component of the velocity along a horizontal line through the cavity center.

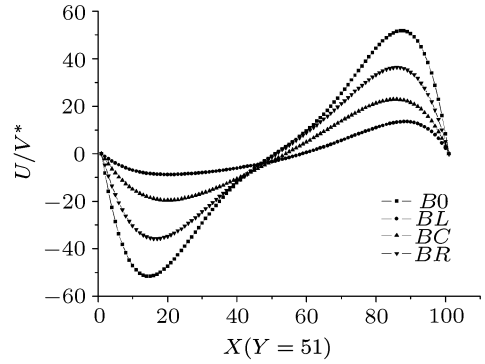


Fig.10. The horizontal component of the velocity along a vertical line through the cavity center.

Meanwhile, we can also find that the horizontal component of velocity is quenched due to the existence of the high magnetic field in Fig.10. The trends of horizontal velocity quenching are the same as that of vertical components, namely, decreasing through BL, BC to BR. The comparison of Figs.9 and 10 show that the quenching efficiency of vertical velocity is larger than that of horizontal velocity. The linear-like velocity profiles in the core of the vortex indicate the uniform vorticity, which is tested in Figs.7(c) and 7(d). Figures 9 and 10 also show that the components of velocity along the central line of the cavity approaches to zero at the same position (center of the cavity) for BL, BC and BR, except the left one with a slight departure.

4.4. Parameter analysis

For further comparison, four flow parameters are listed in Table 2.

As shown in Table 2, the values of the flow parameters in three different positions are all smaller than those of magnetic-field-free case and become weaker from left to right. The results also show that the quenching efficiencies of natural convection in the three different positions are different from one another and the influence of the high magnetic field is very effective, which is in agreement with the conclusion drawn in Subsection 4.2.

Table 2. Flow parameters under the high magnetic field, compared with those without applying magnetic field.

grid 101×101	$\overline{Nu}$	$u_{\max}/V^*$	$v_{\max}/V^*$	$\psi_{\max}$
$B0$	6.5091	51.7334	127.3445	0.002
BL	1.8458	13.4342	18.5698	0.00055
BC	2.6958	22.8781	33.9459	0.00095
BR	3.4037	36.3949	47.0256	0.0014

5. Conclusion

This paper has improved the thermal lattice Boltzmann scheme proposed by Eggels and Somers by proposing a new equilibrium solution for temperature distribution function on the assumption that flow is incompressible. And the statistic definition of macroscopic temperature has been modified accordingly. In addition, a non-equilibrium extrapolation scheme with second accuracy has been adopted for velocity and temperature at the boundaries. This accuracy coincides with the ensemble of the lattice Boltzmann method. Moreover, this boundary condition has other advantages, such as simplicity in computation and facility of algorithm. The improved TLBM has been used to simulate the natural convection of air in a square cavity in Section 3 and the various parameters obtained in the simulation are consistent with the results of other numerical methods. It indicates that the improved TLBM enables the simulations of non-isothermal flows.

Based on the simulation of the natural convection of air, this paper has also carried out the simulation of the natural convection of a solution under the high magnetic field using the improved scheme in order to extend its application to the biological field. The convection of the aqueous solution of KCl (11wt%), which is considered as a diamagnetic fluid with electrically low-conducting, has been investigated under the high magnetic field. In this case, besides the buoyancy, the magnetization force, which can weaken the gravity and offer a micro-gravity condition, is imposed on the liquids because of the gradients of the magnetic induction. Moreover, the convection also is proved to be influenced by the Lorentz force due to the electrically low-conducting.

Three different cases, where the cavity is located on the different zones of the magnetic field, have been studied in the tests. From the results obtained in Section 4, the conclusions are drawn as follows:

(i) The quenching efficiency of the convection in the three cases is different from each another, that is, the left-placed case is the strongest, the right-placed case is the weakest, and the symmetrical-line placed case is weaker than the left case but stronger than the right case.

(ii) The above results are caused by the different distributions of the magnetic induction, i.e. on which side of the symmetry central line of the magnetic field. The direction of the radial component of the magnetic induction on the left side of the magnetic field is along the negative direction of the horizontal axis, and it reverses for the magnetic induction on the right side of the magnetic field.

(iii) The difference between the direction of the radial components of the magnetic induction results in the changes of the directions of the magnetization force and the Lorentz force that points to axes in the horizontal direction, which can quench the convection differently, i.e., the left case is the strongest and the right case is the weakest.

(iv) The quenching efficiency of the convection under the high magnetic field is larger in vertical direction than that in horizontal direction.

Therefore, the presence of the magnetic field, the gravity can be weakened sufficiently and the quenching of the convection is very efficient, which can offer a ground-based micro-gravity trail to study the fluid flow. Damping of natural convection is very important to high quality crystal growth which is very expensive in space. So the ground-based micro-gravity environment produced by a superconducting magnetic field will be a cheaper alternative. The simulation about the phenomena is of great value for the material processing and heat transfer engineering applications.

Acknowledgements

The authors would like to thank Prof. Qian Yue-Hong of Shanghai University, Prof. Guo Zhao-Li of Huazhong University of Science & Technology and Prof. Chen Xiao-Peng of Northwestern Polytechnical University for helpful discussions.

References

[1] Wolf-Gladrow D A 2000 *Lattice–Gas Cellular Automata and Lattice Boltzmann Models: An Introduction* (Berlin, Heidelberg: Springer-Verlag) p2

[2] Hou S L, Zou Q, Chen S, Doolen G and Cogley A C 1995 *J. Comput. Phys.* **118** 329

[3] He X, Chen S and Doolen G D 1998 *J. Comput. Phys.* **146** 282

[4] McNamara G and Alder B 1993 *Physica* A **194** 218

[5] Alexander F J, Chen S and Sterling J D 1993 *Phys. Rev.* E **47** R2249

[6] Chen Y, Ohashi H and Akiyama M 1994 *Phys. Rev.* E **50** 2766

[7] McNamara G, Garcia A L and Alder B J 1995 *J. Statist. Phys.* **81** 395

[8] Bartoloni A, Battista C, Cabasino S, Paolucci P S, Pech J, Sarno R, Todesco G M, Torelli M, Tross W, Vicini P, Benzi R, Cabibbo N, Massaioli F and Tripiccione R 1993 *Int. J. Mod. Phys.* C **4** 993

[9] Shan X 1997 *Phys. Rev.* E **55** 2780

[10] Eggels J G M and Somers J A 1995 *Int. J. Heat and Fluid Flow* **16** 357

[11] Lallemand P and Luo L S 2003 *Phys. Rev.* E **68** 036706

[12] Feng S D, Zhong L H, Gao S T and Dong P 2007 *Acta Phys. Sin.* **56** 1238 (in Chinese)

[13] Lu Y H and Zhan J M 2006 *Acta Phys. Sin.* **55** 4774 (in Chinese)

[14] Somers J A 1993 *Appl. Sci. Res.* **51** 127

[15] Guo Z L, Zheng C G, Li Q and Wang N C 2002 *Lattice Boltzmann Method for Hydrodynamics* (Wuhan: Hubei Science Press) p58 (in Chinese)

[16] Chai Z H, Shi B C and Zheng L 2006 *Chin. Phys.* **15** 1855

[17] van Treeck C, Rank E, Krafczyk M, Tolke J and Nachtwey B 2006 *Computers & Fluids* **35** 863

[18] Orazio A D, Corcione M and Celata G P 2004 *Int. J. Thermal Science* **43** 575

[19] G De Vahl Davis 1983 *Int. J. Numer. Methods Fluids* **3** 249

[20] G Barakos, E Mitsoulis and D Assimacopouls 1994 *Int. J. Numer. Methods Fluids* **18** 695

[21] Wakayama N I, Zhong C W, Kiyoshi T, Itoh K and Wada H 2001 *AIChE Journal* **47** 12 2640

[22] Lee H G, Ha M Y and Yoon H S 2005 *Int. J. Heat and Mass Transfer* **48** 5297

[23] Wu Q F and Li H 2007 *Magnetohydrodynamics* (Changsha: National University of Defense Technology Publishing House) pp50–51 (in Chinese)

[24] Chen X W and Shi B C 2005 *Chin. Phys.* **14** 1398